Accepted Manuscript

Effect of processing parameters on the densification, microstructure and crystallographic texture during the laser powder bed fusion of pure tungsten

A.T. Sidambe, Y. Tian, P.B. Prangnell, P. Fox

Effect of processing parameters on the densification, microstructure and crystallographic texture during the laser powder bed fusion of pure tungsten

Authors: A. T. Sidambe[1,a] , Y. Tian[2,3], P. B. Prangnell[3], P. Fox[1]

1. Department of Mechanical, Materials and Aerospace Engineering, School of Engineering, University of Liverpool, Brownlow Hill, Liverpool, L69 3GH, United Kingdom

2. Department of Engineering, Lancaster University, Lancaster, LA1 4YW, United Kingdom

3. School of Materials, University of Manchester, Manchester M13 9PL, United Kingdom

a. Corresponding author: Alfred T. Sidambe, Department of Mechanical, Materials & Aerospace Engineering, School of Engineering, University of Liverpool, Brownlow Hill, Liverpool, L69 3GH, United Kingdom, Email: A.Sidambe@liverpool.ac.uk, Tel: (+44) 0151 794 6832, Fax: (+44) 0151 794 4703

Abstract

Laser Powder Bed Fusion is a leading additive manufacturing technology, which has been used successfully with a range of lower melting point materials (titanium alloys, nickel alloys, steels). This work looks to extend its use to refractory metals, such as those considered in this paper where the behaviour of pure tungsten powder is investigated. A strategy for fabricating high density parts was developed by creating a process map in which the effect of laser energy density was studied. The process quality was assessed using different techniques including light optical microscopy, XCT, SEM and EBSD. The results showed that the laser energy density was adequate to process tungsten to produce functional parts. The bulk density and optically determined densities, under different process conditions, ranged from 94 to 98%, but there was evidence of micro cracks and defects in specimens due to micro- and macro-scale residual stress. Analysis of the microstructure and local crystallographic texture showed that the melt pool formed under the laser beam favoured solidification in a preferred orientation by an epitaxial growth mechanism. The EBSD local texture analysis of the tungsten specimens showed a <111> // Z preferential fibre texture, parallel to the build direction.

Keywords: Laser Powder Bed Fusion, Selective Laser Melting, Tungsten, Refractory metals, Additive Manufacturing, High-temperature, 3D printing

1. Introduction

Laser Powder Bed Fusion (LPBF) is an additive manufacturing (AM) process that is increasingly being adopted by various industrial sectors to lower the cost of production of components with complex topography, particularly for high value low volume manufacturing and for complex shapes. LPBF is rapidly emerging as an alternative to conventional methods, such as machining and casting, in applications where near net shape components are utilised [1-4]. The LPBF process also has the ability to fabricate functional, custom specific, solid or lattice components with short lead times without the need for tooling [1]. In the LPBF system, a laser with a typical power of at least 200W is used to fuse metal powder into a solid component using data from a sliced 3D CAD file, one layer at a time. The layer thickness is generally in the range of 30 to 50µm [5-9]. The LPBF process is also often referred to as Selective Laser Melting (SLM) and more details about the process have been described elsewhere [1].

Tungsten (W) has a number of special physical properties, such as the highest melting temperature, density and lowest thermal expansion coefficient of any pure metal, which makes it an ideal choice for ultra-high temperature and radiation shielding applications within many technology fields such as military, electro vacuum, crucible, heating elements and pinhole collimators [10, 11]. Hence, there is an increased interest of using the LPBF process to fabricate pure tungsten

3

components, as well as other refractory metal systems. The processing of tungsten via LPBF, although technically challenging, is expected to lead to an advantage in the high value manufacturing sectors such as medical equipment and defence [12, 13]. This advantage is brought about because LPBF has the ability to manufacture complicated shaped tungsten parts with small dimensions, something which cannot be easily achieved using traditional techniques such as casting, forging, or machining, because of the high hardness, brittle nature and high temperature strength capability of tungsten [10].

Physical properties	Tungsten
Density at 25 °C (g/cm^3)	19.2
Liquid Density (g/cm^3)	17.6
Melting Point (°C)	3422
Thermal Conductivity (W.m^{-1}.K^{-1})	174
Melt Viscosity (mPa.s)	8
Ductile-to-brittle transition temperature (°C)	250 to 400
Surface tension Force (N/m)	2.361

Table 1: Physical properties of tungsten [12, 14-16].

Table 1 shows the physical properties of tungsten. Of particular interest are the comparatively high density, high melting point and the high thermal conductivity,

which are expected to contribute to the difficulties of processing tungsten via LPBF. The high melting point of tungsten has been reported to contribute to a high cohesive energy and high surface tension which, in turn, contribute to poor process stability in LPBF, whereas the ductile-to-brittle transition temperature (DBTT) renders tungsten susceptible to cracking from the build-up of residual stresses [12, 17]. In addition to the above mentioned properties, optimisation of the processing of tungsten using LPBF is also made difficult by the large number of process variables in LPBF and its non-equilibrium nature, which requires an in-depth understanding of the process-material interactions [18].

In order to overcome the challenges of manufacturing tungsten components using conventional methods, there have been a number of studies carried out to investigate the use of additive manufacturing. In an early investigation, Zhong et al. [19] reported that a collimator was successfully fabricated using a tungsten nickel alloy powder in a directed energy deposition (DED) blown powder process (Laser Engineered Net Shaping: LENS™). However, pure tungsten powder could not be successfully used due to the metal's high melting point [19]. Later, Ebert et al. used pulsed-laser micro sintering in a study which demonstrated that the density of tungsten parts increased with the applied laser energy [20]. A year later, Deprez et al. successfully fabricated a more complex MR-compatible collimator with a large number of oblique pinholes from pure tungsten powder using LPBF [11]. More

5

recently, the intrinsic physical properties of tungsten and the laser processing parameters have been established as being important in controlling the physical properties of parts produced by the LPBF process. These studies also identified oxidation as a phenomenon that can hinder successful tungsten LPBF processing, which must be avoided [12, 21-24].

In this study, we expand on our recent work [14, 25], and identify further the barriers that limit the effectiveness of LPBF processing of pure tungsten. The overall aim of the work was to use 'process maps' as a basis to more systematically evaluate the relationships between the process variables and part quality. The results have been quantified in terms of the part density and nature of the defects produced, as well as their microstructure and crystallographic texture.

2. Experimental

Plasma-spheroidised commercial purity tungsten powder supplied by Tekna Advanced Materials (Macon, France) was used for producing the test pieces in a Renishaw AM125 LPBF system (Stone, UK). Figure 1 (a) shows a scanning electron microscope (SEM) image of the highly spherical morphology of the powder and Figure 1 (b) shows the powder particle size distribution (PSD). SEM analysis was carried out using a Jeol 6610 (Akishima, Japan) scanning electron microscope at 20kV. Table 2 shows the chemical composition of the powders, as documented in the

6

supplier's powder certification. It can be seen from Table 2 that the initial levels of oxygen in the powder are low at 0.009 wt %. and the powder has high purity with >99.9 wt % comprising of tungsten.
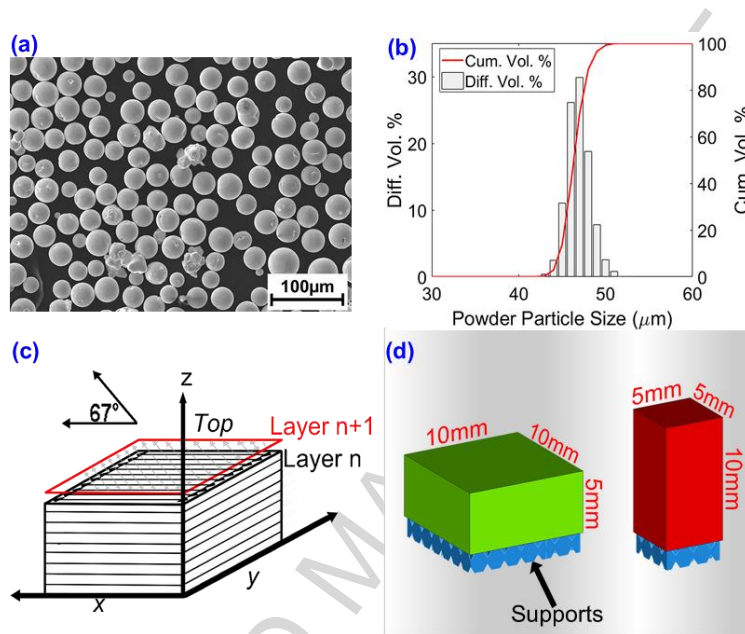

Figure 1: (a) Powder morphology, (b) powder particle distribution for tungsten, (c) illustration of the spatial reference system including the 'meander' scan strategy used and (d) CAD illustration of the test specimens manufactured.

Composition (wt%)						
W	Al	Ta	Ti	O	Mo	Residual
>99.9	0.001	0.003	0.001	0.009	0.003	<0.001

Table 2: Chemical composition of the tungsten powder used in the LPBF processing.

7

The tungsten powder was melted in an argon atmosphere with an initial residual oxygen content of less than 1800 ppm (0.18%). The Renishaw AM125 system operates on the principal of digital beam scanning and uses a high-powered ytterbium fibre laser, with a wavelength of 1070 nm, a maximum laser power of 200 W in continuous wave mode, a maximum laser scanning speed of 2000 mm/s and a laser beam diameter of 43μm at the target surface. A commercially pure titanium substrate was used for the LPBF experiments as a tungsten plate was not available. The use of titanium also reduced the energy required to melt the first few layers, when the plate was cold, creating a good bond between the built part to the plate. Careful consideration, as shown is previous studies [26], is needed when selecting the substrate material as its thermal properties have been reported to significantly affect the LPBF process, particularly through influencing the size of the melt pool and the solidification rate [26].

The laser-based melting of the tungsten powder was carried out by fabricating two types of tungsten specimens. Several square section blocks measuring L=10 mm, W=10 mm and H=5 mm, and L=5 mm, W=5 mm and H=10 mm were manufactured for density, microstructural and XCT measurements, as shown in Figure 1 (d). A 'snaking', also often referred to as the meander, scan strategy was used for each build where the angle of the laser was rotated by 67° between each layer, as

illustrated in Figure 1 (c). Table 3 provides a summary of the six sets of processing parameters used to manufacture the different tungsten LPBF test samples using a constant laser power of 200W, exposure time of 200μs and layer thickness of 50μm. The controlled processing parameters investigated were hatch distance (or spacing) and point distance. The specimens were subsequently named S1HD1 to S2HD3, where S is the scanning speed and HD is the hatch distance. The input laser energy was calculated and derived from the 3 dimensional (3D) specific energy input [27-30]:

$$\varepsilon_{Density} = \frac{P_{Laser}}{v_{scan} \cdot S_{hatch} \cdot t_{layer}} \qquad Eqn \ 1$$

where; $\varepsilon_{Density}$ is the 3D input laser energy density, P_{laser} is the laser power, v_{scan} is the laser scan speed, S_{hatch} is the hatch spacing and t_{layer} is the layer thickness.

After fabrication, the top and build directional surfaces of the tungsten block specimens were analysed using SEM. The Archimedes principle was used to measure the bulk density of the specimens. Specimens were then sectioned, ground, polished to 1μm using an Al_2O_3 powder suspension and analysed for porosity levels using light optical microscopy (LOM). Image processing software, ImageJ, was used to calculate the optically determined density (ODD). A selection of the polished specimens were then subjected to electrolytic etching using a 5% sodium hydroxide solution in a cooled electrolytic cell, at a typical temperature of -20°C at 40V, for microstructural analysis by optical microscopy. The etched specimens were also

9

analysed using SEM (using an acceleration voltage of 20kV) to study the microstructure of the tungsten.

X-Ray computed tomography (XCT) scanning of LPBF tungsten specimens was carried out on the as built samples in order to study the distribution and 3D nature of the various types of defects. However, due to the high density of tungsten, this work was performed on smaller pillars measuring 1 mm × 1 mm × 5 mm which were sectioned from the test blocks. The XCT work was conducted in a Nikon XTH 225 tomographic system (by Nikon Metrology UK Ltd) at the Henry Moseley X-ray Imaging Facility (Manchester, UK) using an accelerating voltage of 200 kV, current of 170 μA, 1s exposure time with a 1 mm thick Sn filter to achieve a voxel size of 5 μm. The defects present were segmented and visualised using the software package FEI Avizo 9.1.

Specimen	Hatch Distance (mm)	Point Distance (μm)	Exposure Time (μs)	Apparent Speed (mm/s)	3D Vol. energy density (J/mm^3)
S1HD1	0.115	20	200	100	348
S1HD2	0.135	20	200	100	296
S1HD3	0.155	20	200	100	260
S2HD1	0.115	29	200	145	240

S2HD2	0.135	29	200	145	204
S2HD3	0.155	29	200	145	179

Table 3: Summary of the processing parameters used to manufacture six different tungsten components at 200 W laser power.

To determine the microtexture, EBSD orientation maps were obtained on selected polished x-y build plane and z-y build-directional section specimens (Table 3) using an FEI Sirion SEM (Oregon, USA) equipped with an Oxford Instrument Nordlys EBSD detector (Abingdon, UK). The maps were generated using an acceleration voltage of 20kV and step size range between 1μm and 2μm. Map areas of 800μm by 600μm were measured for the x-y bed plane cross-section views and 600μm x 1500μm for the x-z build direction view.

3. Results and Discussion

3.1. Surfaces

The tungsten blocks were fabricated without any visible defects or delamination during the melting process and a relatively smooth top surface was produced. However, at a higher magnification surface cracks were visible within many of the samples. Figure 2 shows SEM micrographs from the as-built top (x-y; S1HD1 to S2HD3) and the side surfaces (x-z; S1HD1z to S2HD3z) of all the test samples. It

11

can be seen from Figure 2 that the volume of unmelted adherent particles reduced when the tungsten was processed using an increased energy density; i.e. in the sample produced with a point distance of 20 μm and a hatch spacing of 115 μm (Figure 2 (S1HD1)). The individual scan tracks and their directions can be discerned from the solidification ripples seen at the top of the solidified melt pools. The surface topographical texture was found to be different between the top cross-sectional and side build directional surfaces. The level of unmelted adherent particles was very high when viewing the specimens' side surfaces (e.g. x-z) (S1HD1z to S2HD3z). There were surface cracks visible on both the horizontal and build-directional views, as indicated in Figure 2 (S2HD1 and S2HD2z). As 'pure' tungsten has a narrow freezing range, these surface cracks are unlikely to be due to solidification cracking and can be linked to the build-up of residual stresses in the deposit and the material's high elevated temperature strength and inherently low ductility [31, 32]. The thermal stresses within specimens are caused by thermal gradients generated by the heat source, which due to differential contraction on cooling cause large tensile stresses in the plane of the last solidified layers [33]. These residual stresses, formed by thermal contraction, will not readily relax in a material with a high elevated temperature flow strength, which in turn leads to the formation of cracks [34]. Particularly problematic in this regard is the dramatic fall in ductility that arises when the temperature drops below tungsten's unusually high ductile-brittle transition temperature (Table 1).
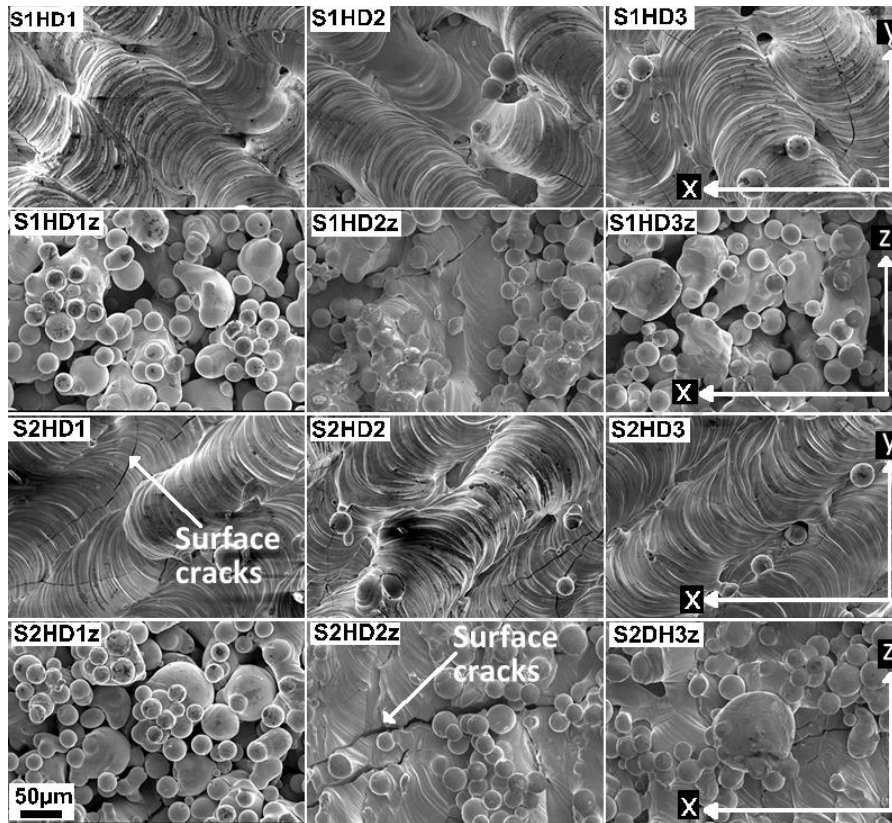
Figure 2: SEM images of the LPBF tungsten test cubes as built (x-y) top surfaces (S1HD1 to S2HD3) and build direction side (x-z) surfaces (S1HD1z to S2HD3z).

3.2. Densification behaviour

3.2.1. X-Ray Tomography

XCT analysis was carried out on selected samples in order to further investigate the internal distribution of the cracks, porosity, and other defects. Figure 3 shows isometric 3D visualisations of the defects segmented in the XCT scans from four tungsten specimens (S1HD1 and S1HD3 in Table 3) taken from two separate LPBF

13

build cycles. The scans show the size and spatial distribution of the pores in 3D within the specimens. It should be noted that the effective resolution is limited because of the high X-ray absorption to discernible porosities and cracks greater than 10µm in thickness. It can be seen in Figure 3 that the volume fraction of the defects appears to increase with increasing build height in sample S1HD1, which was fabricated using a higher laser energy density (particularly from the LPBF build 2). This may indicate that the internal stresses in LPBF can vary depending on position; i.e. in relation to build height. This can be caused by changing conditions within the build chamber, due to the heat flux to the build plate and into the powder bed. The laser heat flux density can also be affected, or attenuated, by powder spatter and metallic vapour, which has been reported to interact with the laser radiation during the LPBF process [35]. This beam interaction behaviour, coupled with instabilities in the powder layer deposition, can lead to difficulties in controlling the process. Variation in the laser induced heat flux and energy density can also lead to locally variable thermal gradients at the layer interface. However, to understand these interactions more fully further investigations would be needed; for example, using W powder with a smaller powder size and distribution (e.g. sub 25 µm) to increase the laser heat flux density absorbed by the powder [36]. In comparison, the samples fabricated using the lower applied laser energy density of 260 J/mm^3, represented by S1HD3, had a larger volume of pores and defects, whereas the overall volume fraction of both pores and defects was lower in S1HD1 (for both build 1 and 2). As

14

can be seen from the higher magnification view of specimen S1HD1, the larger high aspect-ratio defects were found to be irregular in morphology.
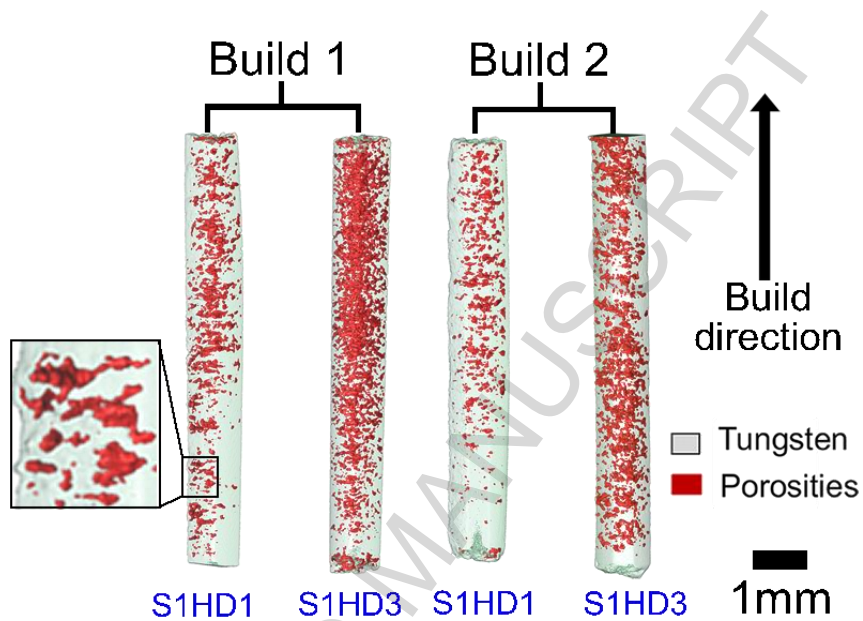

Figure 3: XCT scan results from small rod samples machined from the centre of each cube, showing isometric 3D visualisations of the defects (red) found in four W specimens S1HD1 and S1HD3 (in Table 3) taken from two separate LPBF build cycles.

Cross-sectional views of specimens S1HD1 and S1HD3 confirmed the presence of irregular 'lack of fusion flaws', porosity and cracking along the grain boundaries, as shown in Figure 4. Such 'lack of fusion' defects may be encouraged by the presence of unmelted particles and the unfavourable wetting conditions that have been

15

reported when melting metals such as tungsten [12]. The presence of unmelted

powder particles has also already been shown in Figure 2. In addition, the high

conductivity of tungsten may result in greater variability in the local thermal

conditions. For example, when scanning tungsten over a large area, the laser beam

travels a greater distance, which gives rise to a longer beam return time and

successively scanned tracks have more time to cool down, leading to a lower local

metal temperature [37]. The more successful melting of the powder and the high

densities achieved indicate that higher laser energy densities lead to a significant

benefit, as shown when comparing S1HD1 and S1HD3 in Figure 3 and in Figure 4 (c

and d), where the S1HD1 specimen shows less cracking and porosity. This argument
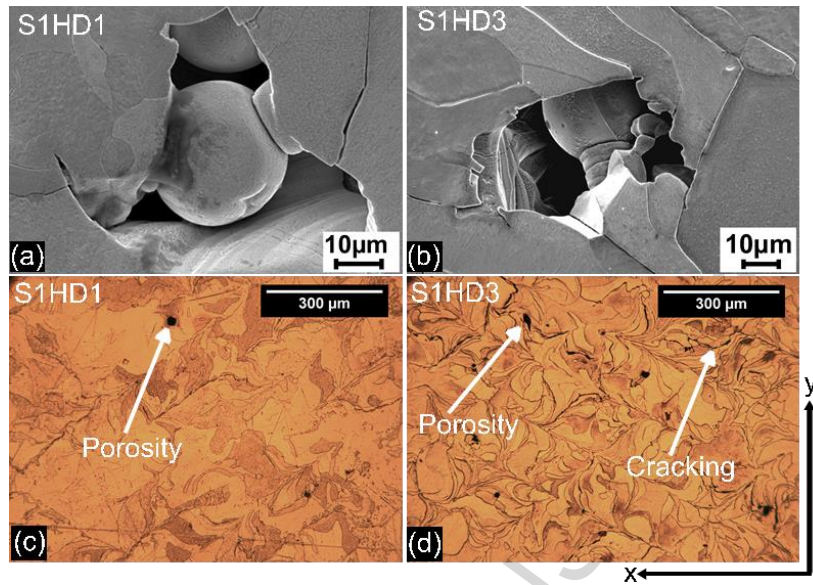
is further expanded on in the next section.

Figure 4: SEM and optical images showing (a) and (b) details of the types of defects found in the test cubes and (c) and (d) the distribution of the porosity and cracks in typical x-y cross-sections (x-y) from the S1HD1 and S1HD3 specimens.

3.2.2. Densification

To better understand the effect of the 3D laser energy density on the densification of the LPBF tungsten test cubes, their bulk density was determined using the Archimedes method and the optically determined density (ODD) was calculated from the porosity area fraction, measured by optical microscopy from the average of (x-y) cross-sections and (x-z) build direction porosities of the polished block specimens. Figure 5 shows results of the density of the specimens fabricated using laser energy densities ranging from 179 to 348 J/mm^3, as shown in Table 3. The

17

corresponding relative sample density results ranged between 95 and 97% for the bulk densities obtained using the Archimedes method. Overall for all the measurement methods it can be seen from Figure 5, that there is a clear correlation between the measured data and the increasing laser energy density, which suggests that a higher energy density leads to less part porosity, up to a limit of 98% with the beam power and process conditions available. Therefore, the tungsten specimens manufactured using this current scan strategy increased in density with increasing laser energy density up to energies of ~ 350 J/mm^3, beyond which it is probably not possible to eliminate the final 2% of defects.
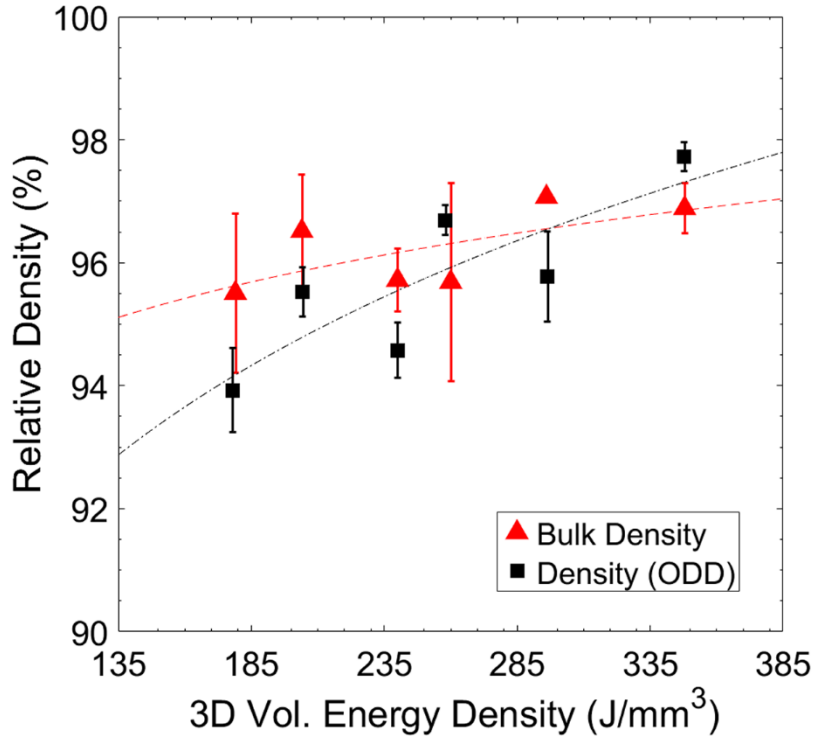
Figure 5: Correlation between processing parameters and the density measured by Archimedes method (bulk density) and from optical micrographs (Density (ODD)).

In this study a relatively small laser beam diameter (43 μm) was used to melt the W powder. A small beam diameter of this magnitude leads to relatively high irradiance levels and an increased heat flux incident on the thin layer of powder [14, 25]. When the heat flux is considered in the direction which is parallel to the build direction, it can be concluded that this was sufficient to fully re-melt the previous layer. In order to ascertain whether these densification levels are suitable for parts that can be used in high performance applications, suitable mechanical testing and performance evaluation would need to be carried out, and this has not been done in

19

this study. It is likely that the number of defects can be reduced by further increasing the laser energy density during processing and this could be achieved by using a finer powder and a narrower particle size distribution (PSD) which would allow the use of a reduced layer thickness.

3.3. Microstructure and analysis

To investigate further the effect of the LPBF processing parameters and the sources of defects, the microstructure of the tungsten specimens was studied. The results of the effect of the processing parameters listed in Table 3 on the microstructure are shown for (x-y) build plane and build direction (x-z) build directional views in Figure 6. Evident in the backscattered SEM images in Figure 6, is the presence of grain boundaries that may act as crack initiation sites in this brittle material. As discussed above, the cracking seen at this microscopic level is thought to be induced by a combination of the thermal stresses within the specimens and the fact that the material is brittle at a temperature below its DBTT.
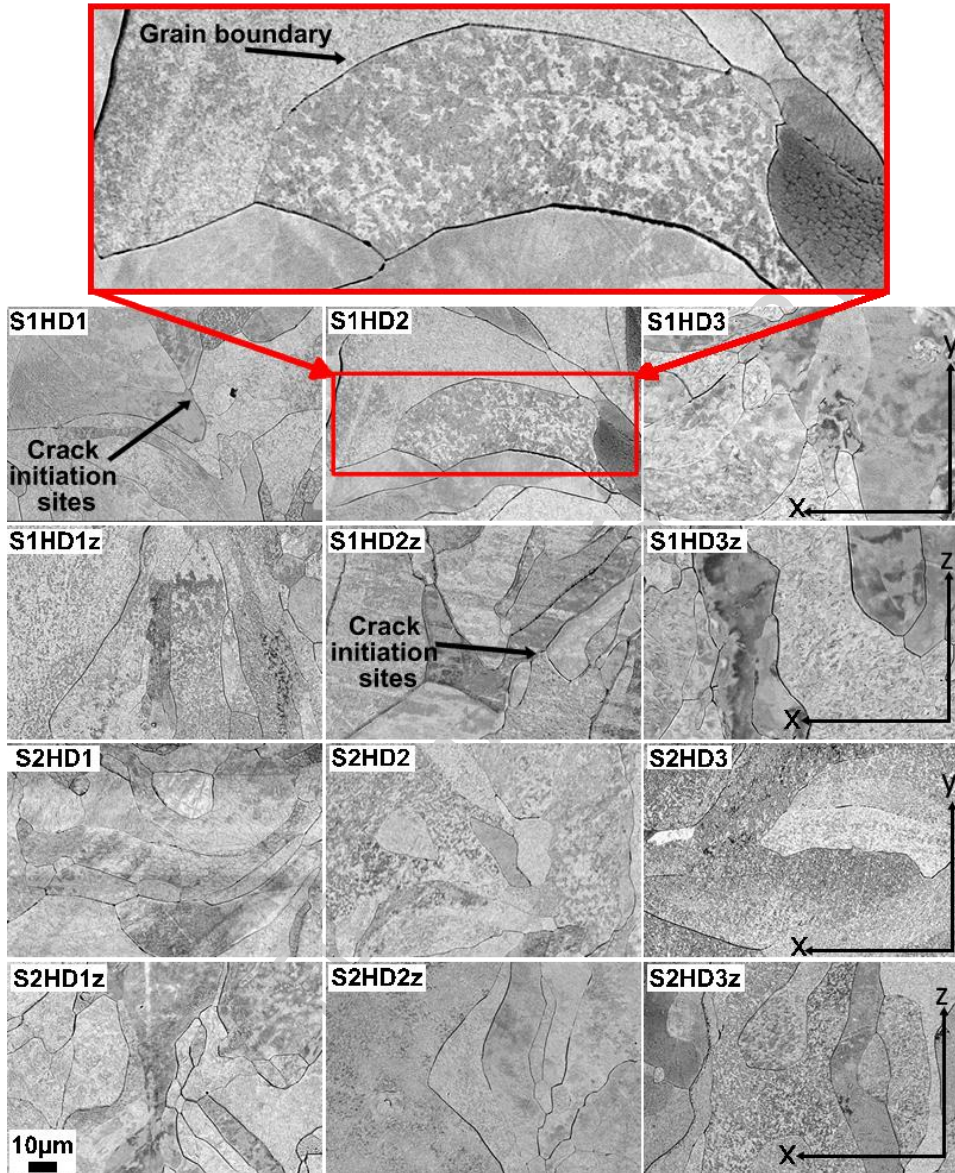
Figure 6: SEM images from etched samples showing typical microstructures taken from centre of each plane from the x-y build plane and x-z build plane cross section views in samples S1HD1 to S2HD3.

21

As already noted, tungsten is highly susceptible to cracking because it has a body-centre cubic (bcc) lattice, and a high melting point, caused by a partial covalent character to its bonding, which leads to a DBTT well above room temperature, typically in the range between 250 to 400°C, Table 3 [17, 38, 39]. In tungsten significant ductile behaviour usually only occurs above 400 °C, and below 250 °C tungsten does not normally show plastic deformation. This leads to cracking if a high enough stress develops. The high yield strength of tungsten at temperature reduces plastic relaxation on cooling, which when combined with a high DBTT makes micro cracking the most likely method to relieve strain. On cooling, the long-range residual stresses generated by the temperature gradients add to any local microstresses generated between neighbouring grains (due to anisotropy in the coefficient of thermal expansion (CTE) and the elastic properties of the bcc unit cell). The cracking in tungsten alloys has been reported to be a function of the grain structure and texture, which may create a significant problem for LPBF as it produces directional columnar grain growth [34].

In LPBF processing the grain structure is normally anisotropic with the solidification conditions favouring elongated columnar grain structures in most alloy systems. This type of grain structure is particularly favoured by alloys with a low freezing range, such as pure metals and Ti-6V-4Al, which do not develop sufficient constitutional super-cooling to allow nucleation ahead of the solidification front [40-

43]. In this scenario grains regrow epitaxially from the fusion boundary and their growth direction is generally controlled by the shape of the melt pool and raster strategy [43]. In metals there is also a generally a preferential crystallographic growth direction, which leads to a crystallographic texture by the competitive growth of favourably orientated grains [43]. It is difficult to see how this columnar structure and texture can be removed from materials produced by sequential melting of layers, as it would require the blocking of the regrowth of pre-existing grains to disrupt the columnar structure. In conventional processing heat treatments after cold working are often used to produce recrystallization, modifying the grain structure. With near net shaped components this method is not available as it is not possible to create the high dislocation density required. Also lacking in tungsten are any phase changes that could be used to modify the grain structure. Therefore, any heat treatments would only lead to a slow increase in grain size.
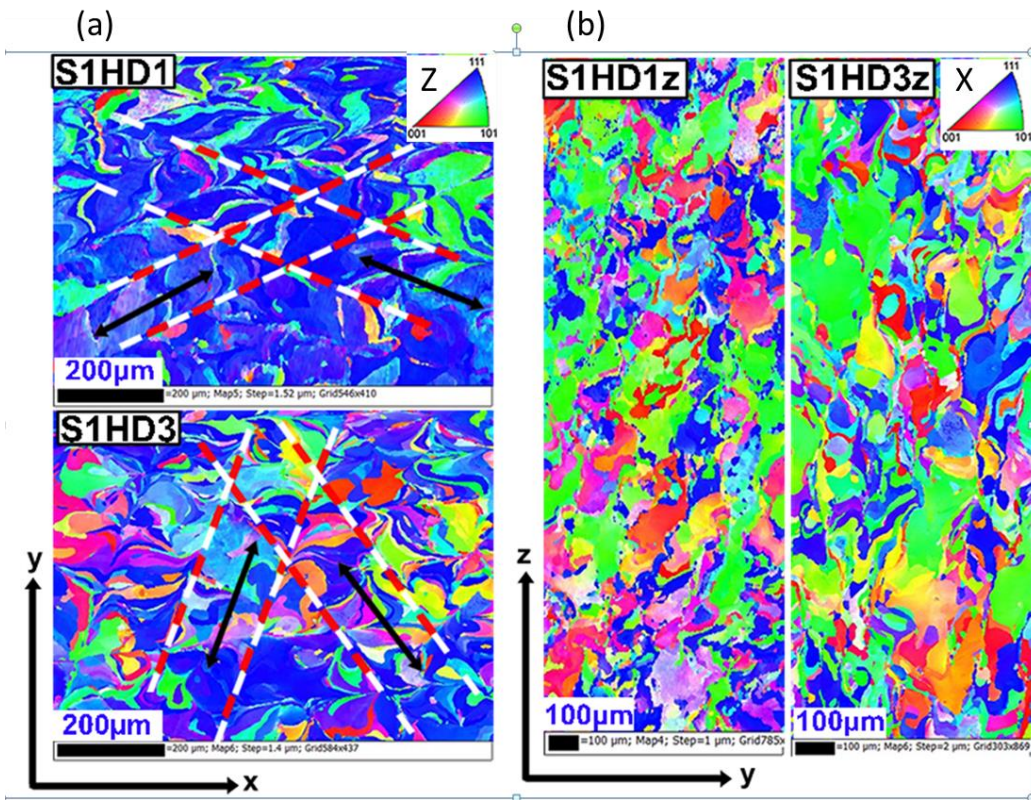
3.4. Local crystallographic texture (EBSD)

Figure 7: EBSD Inverse pole figure (IPF) orientation maps of the S1HD1 and
S1HD3 samples show in (a) x-y cross sections and (b) x-z vertical cross-section
views. The IPF colouring is relative to the plane normal direction (i.e. in (a) parallel
to Z the build direction and (b) parallel to x).

To provide further insight into the melt pool solidification and preferred grain growth orientations, the local crystallographic texture of the specimens was analysed using EBSD. Figure 7 shows EBSD IPF orientation maps for tungsten specimens, viewed in both the x-y and x-z planes, fabricated using the laser energy densities of 348 and 260 J/mm^3. Further EBSD data are provided in Figure 8 which compares the high angle grain boundaries (>15° shown as black lines) and the grain size distributions in the x-y plane for samples S1HD1 and S1HD3. It can be noted from Figure 7 and Figure 8 that when a lower laser energy density of 260 J/mm^3 was used, it is easier to discern an influence on the texture from the previously melted layer (or layers) and the 67° rotation scanning pattern.

The formation of long columnar grains along the build direction was confirmed when analysing the maps in the vertical sections seen in Figure 7 (b). This result is expected because LPBF, and other variants of AM such as electron beam melting, are layer by layer deposition, moving melt pool processes, which have been reported to lead to epitaxial and competitive re-growth of columnar grains. This is particularly the case in pure metals where little constitutional supercooling is possible to encourage nucleation in the melt ahead of the solidification front [40-43]. The preferential grain growth can also give rise to a solidification texture (see below) which when combined with a columnar grain structure can produce anisotropy in the mechanical properties of AM deposits with refractory metals [43, 44]. During the

25

LPBF process, part of the underlying solid material; i.e. the previously deposited layer, is re-melted and provides a substrate from which solidification can occur. Although there is a nucleation energy barrier to the formation of new grains, there is no barrier to the regrowth of pre-existing grains, especially in a pure metal, and solidification occurs by continued growth of the pre-existing grains present at the fusion boundary [43, 45]. These grains grow competitively in the same way as columnar grains in conventional casting, the fastest growing crystals out competing their neighbours. The fastest growth direction is parallel to the maximum thermal gradient at the solidification front which is normal to the rear melt pool surface and thus influenced by the melt pool shape and raster strategy. A relatively wide melt track was selected to build the tungsten parts (top surfaces Figure 2) in order to reduce cracking by generating shallower thermal gradients, and it is thought this may have led to the larger grain sizes, seen in Figure 8. The rotation strategy also led to perturbations in the direction of growth between layers, as can be seen in Figure 7(b), from the change in scan direction. Strong alignment of the grain structure and variation in the texture can also be seen with raster directions in the x-y plane views in Figure 7 and Figure 8.
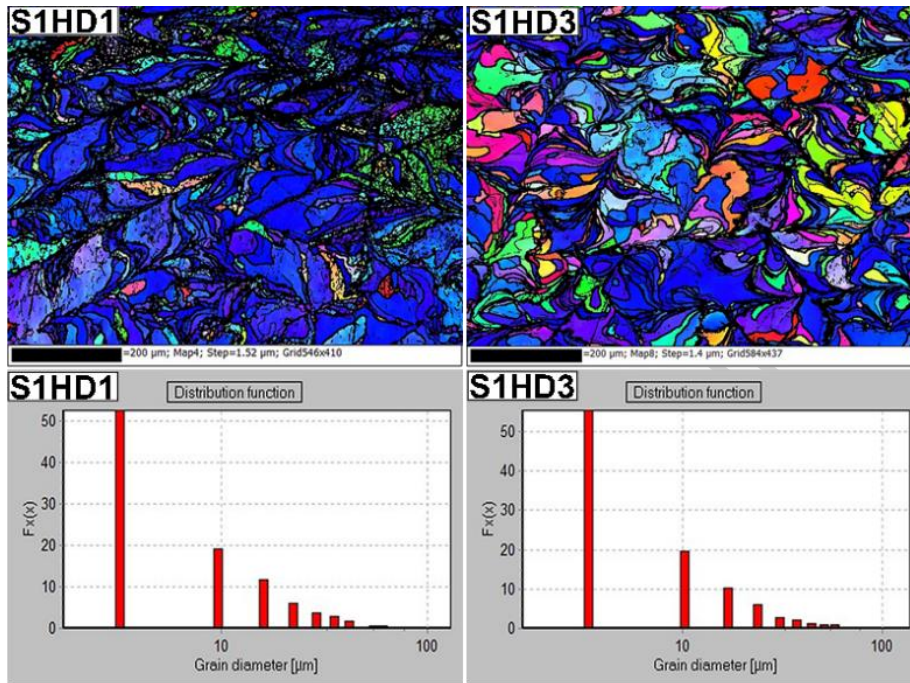
Figure 8: EBSD map showing high angle grain boundaries (>15°) as black lines map (top) and the grain size distributions in the x-y plane measured from each map (bottom) for samples S1HD1 and S1HD3.

The grain size distributions of the tungsten (S1HD1 and S1HD3) are illustrated in Figure 8, in which the high angle grain boundaries (HAGBs) are highlighted by black lines (top figures). In addition, the grain diameter size-frequency distributions are depicted in the bottom figures of Figure 8. From the distribution plots in Figure 8, it was found that the majority of the grains had a diameter below 10 μm in both the specimens, when analysed in the x-z build plane. The average grain sizes were very similar being equal to 11.8 μm for S1HD1 and 11.3 μm for S1HD3. However, the maximum grain diameter was larger at 153 μm for S1HD1 in comparison to 137 μm

27

for the S1HD3 specimen. In the EBSD data in Figure 7 in the x-z plane maps, coarser regions of similar texture can also be noted in sample S1HD3z compared to S1HD1z (in spite of the slightly different magnification scales between S1HD1z and S1HD3z). The results show that increasing the hatch distance to 155μm, and so decreasing the laser energy density led to coarser columnar grains. This suggests the maximum grain diameter is influenced by the melt-pool overlap between neighbouring tracks; i.e. when the hatch spacing is increased the re-melted grains from the previous pass will tend to grow into the melt pool from the next track to a distance controlled by the re-melted width.

Pole figures depicting the textures taken from the cross-sectional view (x-y) EBSD maps for samples S1HD1 and S1HD3 are depicted in Figure 9. The pole figures for both samples show similar textures with the presence of a strong common 111 orientation aligned with Z, the build direction, (maximum intensity of 10 times random). For samples S1HD1 there is a fairly uniform distribution of poles around this axis. The texture can thus best be described as <111>//z fibre texture. However, for sample S1HD3 there is a stronger single component <111> with a 111 pole also aligned close to Y in the transverse direction, using the build reference frame this component can be described as {111}<0$\bar{1}$1>. However, this alignment may be coincidence and the result of the large grain size relative to the EBSD map area.

Preferential growth in the <111> direction is unusual in BCC metals, which are generally reported to have a preferred <100> growth direction during solidification and to have a <001>//Z fibre texture in powder bed AM with materials like titanium [17, 38, 45]. The origin of the different texture observed here is currently unclear and needs further investigation. However, other preferred texture components have been noted in AM processes and attributed to adjustment of the preferred growth direction in response to systematic changes in the raster direction between beam passes. For example, in DED systems rotated cube and <110>//Z components have been observed [46, 47]. In AM the <001>//Z fibre texture is most typically observed in powder bed systems where the melt pool is shallow and elongated because of a high scanning speed and low material conductivity (i.e. in titanium EBM [40]). Antonysamy et al. [40] proposed this occurs because the rear of the melt pool is at a shallow angle and therefore the preferred growth direction (normal to the melt pool surface) is not greatly tilted relative to Z, so that when rastering occurs in orthogonal directions in alternate layers, grains are selected that have an average preferential growth direction of <001> aligned with Z. In other AM processes with a deeper, more bowl-shaped melt pool, the angle between the preferred crystal growth direction and Z will increase (i.e. the grains become more tilted), so that in response to rastering, alternating dendrite sidearm growth may establish an alternative stable preferred orientation after several layers (e.g. the 'rotated cube' or <110>//Z seen in DED [47]). As W has a high thermal conductivity and high liquid surface tension, it

29

is likely that this will also produce a more bowl shaped melt pool with a more inclined solidification front relative to Z than for materials like titanium, and when combined with the rotation of the beam path every layer this could explain why this unusual texture is seen in this case. It may also be noteworthy that the angle between {111} planes in BCC metals is $\sim 70^0$, which is close to the 67^0 rotation angle, which was set on the Renishaw system, and this crystal symmetry may be relevant in selecting the stronger single {111}<$0\bar{1}1$> component seen in sample S1HD3.
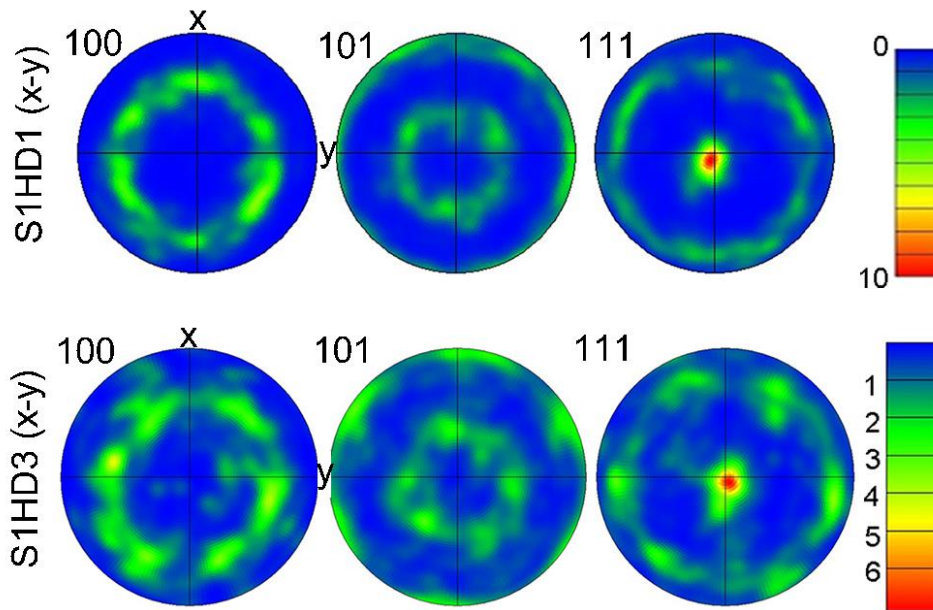

Figure 9: Pole figures depicting the tungsten LPBF textures measured in the (x-y) plane for samples S1HD1 and S1HD3.

4. Conclusion

This study has identified some of the main barriers that limit the effectiveness of LPBF processing of pure tungsten. The effect of key processing parameters has been demonstrated by establishing a process window in which test samples could be built with satisfactory visual quality, with a varied laser energy density.

The quantification of part integrity, in terms of porosity, defects, and density, showed that our strategy was able to melt the tungsten powder and that an increase in laser energy density was accompanied by an increase in the relative density of the parts. Although some of the specimens were susceptible to cracking, relative densities of up to a limit of 98% were achieved by increasing the laser energy density up to 350 J/mm^3. Overall, the density and quality of the W specimens fabricated in this study are sufficiently high for use in applications such as the medical radiation shielding and in nuclear imaging, where W collimators are widely used, and in other plasma facing environments. This has the advantage that LPBF of tungsten can produce components and parts with high levels of complexity and accuracy, which are impossible to produce using conventional methods.

Analysis of the microstructure, global and local crystallographic texture showed a columnar grain structure generated by an epitaxial re-growth mechanism, as noted in other AM processes with pure metals. Using a laser energy density of up to 348

31

J/mm^3 led to samples showing an unusual strong <111> // Z fibre texture. It is postulated this may be related to the deeper melt pool shape than normally seen in LPBF because of the high thermal conductivity and surface tension of tungsten, combined with the 67º raster direction rotation employed between deposited layers in the Renishaw AM machine.

The outcomes of this research have demonstrated that the laser processing parameters in LPBF can be tailored to fabricate parts with relatively high densities. This research shows how the application of refractory metals in additive manufacturing can be used to lower the cost of production, particularly for high value low volume manufacturing and for complex shapes.

5. Acknowledgements

6. References

[1] Sidambe AT. Biocompatibility of Advanced Manufactured Titanium Implants-A Review. Materials. 2014;7:8168-88. https://doi.org/10.3390/ma7128168.

[2] Andani MT, Shayesteh Moghaddam N, Haberland C, Dean D, Miller MJ, Elahinia M. Metals for bone implants. Part 1. Powder metallurgy and implant rendering. Acta Biomater. 2014;10:4058-70. https://doi.org/10.1016/j.actbio.2014.06.025.

[3] Fox P, Pogson S, Sutcliffe CJ, Jones E. Interface interactions between porous titanium/tantalum coatings, Selective Laser Melting (SLM), on a cobalt–chromium alloy. Surface & Coatings Technology. 2008;202:5001–7. https://doi.org/10.1016/j.surfcoat.2008.05.003.

[4] Sidambe AT, Todd I, Hatton PV. Effects of build orientation induced surface modifications on the in vitro biocompatibility of electron beam melted Ti6Al4V. Powder Metall. 2016;59:57-65. https://doi.org/10.1080/00325899.2016.1153278.

[5] Ivanova O, Williams C, Campbell T. Additive manufacturing (AM) and nanotechnology: promises and challenges. Rapid Prototyping J. 2013;19:353-64. https://doi.org/10.1108/Rpj-12-2011-0127.

[6] van Noort R. The future of dental devices is digital. Dent Mater. 2012;28:3-12. https://doi.org/10.1016/j.dental.2011.10.014.

[7] Harrison NJ, Todd I, Mumtaz K. Reduction of micro-cracking in nickel superalloys processed by Selective Laser Melting: A fundamental alloy design

33

approach. Acta Materialia. 2015;94:59-68.

https://doi.org/10.1016/j.actamat.2015.04.035.

[8] Vora P, Mumtaz K, Todd I, Hopkinson N. AlSi12 in-situ alloy formation and residual stress reduction using anchorless selective laser melting. Additive Manufacturing. 2015;7:12-9. https://doi.org/10.1016/j.addma.2015.06.003.

[9] Sidambe AT. Effects of build orientation on 3D-printed Co-Cr-Mo: surface topography and L929 fibroblast cellular response. The International Journal of Advanced Manufacturing Technology. 2018. https://doi.org/10.1007/s00170-018-2473-0.

[10] Li R, Qin M, Liu C, Huang H, Lu H, Chen P, et al. Injection molding of tungsten powder treated by jet mill with high powder loading: A solution for fabrication of dense tungsten component at relative low temperature. International Journal of Refractory Metals and Hard Materials. 2017;62, Part A:42-6. https://doi.org/10.1016/j.ijrmhm.2016.10.015.

[11] Deprez K, Vandenberghe S, Van Audenhaege K, Van Vaerenbergh J, Van Holen R. Rapid additive manufacturing of MR compatible multipinhole collimators with selective laser melting of tungsten powder. Med Phys. 2013;40:012501. https://doi.org/10.1118/1.4769122.

[12] Zhou X, Liu XH, Zhang DD, Shen ZJ, Liu W. Balling phenomena in selective laser melted tungsten. J Mater Process Tech. 2015;222:33-42. https://doi.org/10.1016/j.jmatprotec.2015.02.032.

[13] Wauthle R, van der Stok J, Amin Yavari S, Van Humbeeck J, Kruth JP, Zadpoor AA, et al. Additively manufactured porous tantalum implants. Acta Biomater. 2015;14:217-25. https://doi.org/10.1016/j.actbio.2014.12.003.

[14] Sidambe AT, Fox P. Interaction of pure tungsten powder with processing conditions in Selective Laser Melting. POWDERMET2017: International Conference on Powder Metallurgy and Particulate Materials. Las Vegas, Nevada: MPIF; 2017.

[15] Erik L, Wolf-Dieter S. Tungsten: properties, chemistry, technology of the element, alloys, and chemical compounds. New York: Plenum Publishers; 1999.

[16] Paradis P-F, Ishikawa T, Yoda S. Viscosity of liquid undercooled tungsten. J Appl Phys. 2005;97:106101-1--3. https://doi.org/10.1063/1.1896432.

[17] Wang F, Guo W, Liu J, Li S, Zhou J. Microstructural evolution and grain refinement mechanism of pure tungsten under explosive loading condition. International Journal of Refractory Metals and Hard Materials. 2014;45:64-70. https://doi.org/10.1016/j.ijrmhm.2014.03.008.

[18] Rombouts M, Kruth JP, Froyen L, Mercelis P. Fundamentals of selective laser melting of alloyed steel powders. Cirp Ann-Manuf Techn. 2006;55:187-92.

[19] Zhong M, Liu W, Ning G, Yang L, Chen Y. Laser direct manufacturing of tungsten nickel collimation component. J Mater Process Tech. 2004;147:167-73. https://doi.org/10.1016/j.jmatprotec.2003.12.009.

[20] Ebert R, Ullmann F, Hildebrandt D, Schille J, Hartwig L, Kloetzer S, et al.

Laser Processing of Tungsten Powder with Femtosecond Laser Radiation. J Laser Micro Nanoen. 2012;7:38-43. https://doi.org/10.2961/jlmn.2012.01.0007.

[21] Nie B, Yang L, Huang H, Bai S, Wan P, Liu J. Femtosecond laser additive manufacturing of iron and tungsten parts. Applied Physics A. 2015;119:1075-80.

[22] Bai S, Liu J, Yang P, Huang H, Yang L-M. Femtosecond fiber laser additive manufacturing of tungsten. SPIE LASE: International Society for Optics and Photonics; 2016. p. 97380U-U-10.

[23] Ivekovic A, Omidvari N, Vrancken B, Lietaert K, Thijs L, Vanmeensel K, et al. Selective laser melting of tungsten and tungsten alloys. International Journal of Refractory Metals and Hard Materials. 2017. https://doi.org/10.1016/j.ijrmhm.2017.12.005.

[24] Tan C, Zhou K, Ma W, Attard B, Zhang P, Kuang T. Selective laser melting of high-performance pure tungsten: parameter design, densification behavior and mechanical properties. Science and Technology of Advanced Materials. 2018:1-22. https://doi.org/10.1080/14686996.2018.1455154.

[25] Sidambe AT, Fox P. Investigation of the Selective Laser Melting process with tungsten metal powder. 19th Plansee Seminar. Reutte, Austria: Plansee; 2017.

[26] Pogson SR, Fox P, Sutcliffe CJ, O'Neill W. The production of copper parts using DMLR. Rapid Prototyping J. 2003;9:334-43.

[27] Brown B. Characterization of 304L stainless steel by means of minimum input energy on the selective laser melting platform [Masters]: Missouri University Of

Science And Technology; 2014.

[28] Gu D, Shen Y. Balling phenomena in direct laser sintering of stainless steel powder: Metallurgical mechanisms and control methods. Mater Design. 2009;30:2903-10. https://doi.org/10.1016/j.matdes.2009.01.013.

[29] Yang YQ, Lu JB, Luo ZY, Wang D. Accuracy and density optimization in directly fabricating customized orthodontic production by selective laser melting. Rapid Prototyping J. 2012;18:482-9. https://doi.org/10.1108/13552541211272027.

[30] Yadroitsev I, Bertrand P, Smurov I. Parametric analysis of the selective laser melting process. Appl Surf Sci. 2007;253:8064-9. https://doi.org/10.1016/j.apsusc.2007.02.088.

[31] Ren C, Fang ZZ, Koopman M, Butler B, Paramore J, Middlemas S. Methods for improving ductility of tungsten - A review. International Journal of Refractory Metals and Hard Materials. 2018;75:170-83. https://doi.org/10.1016/j.ijrmhm.2018.04.012.

[32] Butler BG, Paramore JD, Ligda JP, Ren C, Fang ZZ, Middlemas SC, et al. Mechanisms of deformation and ductility in tungsten – A review. International Journal of Refractory Metals and Hard Materials. 2018;75:248-61. https://doi.org/10.1016/j.ijrmhm.2018.04.021.

[33] Taylor A. X-ray Metallography. 1961.

[34] Shah DM, Berczik D, Anton DL, Hecht R. Appraisal of other silicides as structural materials. Mat Sci Eng A-Struct. 1992;155:45-57.

https://doi.org/10.1016/0921-5093(92)90311-N.

[35] Liu Y, Yang Y, Mai S, Wang D, Song C. Investigation into spatter behavior during selective laser melting of AISI 316L stainless steel powder. Mater Design. 2015;87:797-806. https://doi.org/10.1016/j.matdes.2015.08.086.

[36] Gusarov AV, Yadroitsev I, Bertrand P, Smurov I. Heat transfer modelling and stability analysis of selective laser melting. Appl Surf Sci. 2007;254:975-9. https://doi.org/10.1016/j.apsusc.2007.08.074.

[37] Kruth JP, Froyen L, Van Vaerenbergh J, Mercelis P, Rombouts M, Lauwers B. Selective laser melting of iron-based powder. J Mater Process Tech. 2004;149:616-22. https://doi.org/10.1016/j.jmatprotec.2003.11.051.

[38] Upmanyu M, Hassold G, Kazaryan A, Holm E, Wang Y, Patton B, et al. Boundary mobility and energy anisotropy effects on microstructural evolution during grain growth. Interface Science. 2002;10:201-16. https://doi.org/10.1023/A:1015832431826.

[39] Vrancken B. Study of residual stresses in selective laser melting. 2016.

[40] Antonysamy AA. Microstructure, texture and mechanical property evolution during additive manufacturing of Ti6Al4V alloy for aerospace applications. 2012.

[41] Kruth J-P, Badrossamay M, Yasa E, Deckers J, Thijs L, Van Humbeeck J. Part and material properties in selective laser melting of metals. 2010.

[42] Antonysamy AA, Meyer J, Prangnell PB. Effect of build geometry on the β-grain structure and texture in additive manufacture of Ti6Al4V by selective electron

beam melting. Mater Charact. 2013;84:153-68.

https://doi.org/10.1016/j.matchar.2013.07.012.

[43] Thijs L, Montero Sistiaga ML, Wauthle R, Xie Q, Kruth J-P, Van Humbeeck J. Strong morphological and crystallographic texture and resulting yield strength anisotropy in selective laser melted tantalum. Acta Materialia. 2013;61:4657-68. https://doi.org/10.1016/j.actamat.2013.04.036.

[44] Shifeng W, Shuai L, Qingsong W, Yan C, Sheng Z, Yusheng S. Effect of molten pool boundaries on the mechanical properties of selective laser melting parts. J Mater Process Tech. 2014;214:2660-7.

https://doi.org/10.1016/j.jmatprotec.2014.06.002.

[45] David SA, Vitek JM. Correlation between solidification parameters and weld microstructures. Int Mater Rev. 1989;34:213-45.

https://doi.org/10.1179/imr.1989.34.1.213.

[46] DebRoy T, Wei HL, Zuback JS, Mukherjee T, Elmer JW, Milewski JO, et al. Additive manufacturing of metallic components – Process, structure and properties. Prog Mater Sci. 2018;92:112-224.

https://doi.org/https://doi.org/10.1016/j.pmatsci.2017.10.001.

[47] Wei HL, Mazumder J, DebRoy T. Evolution of solidification texture during additive manufacturing. Scientific reports. 2015;5:16446.

Highlights

- A strategy for fabricating high density parts was developed by creating a process map in which the effect of laser energy density was studied.

- The process quality was assessed using different techniques including light optical microscopy, XCT, SEM and EBSD.

- The results showed that the laser energy density was adequate to process tungsten to produce functional parts.

- The relative densities, under different process conditions, ranged from 94 to 98% but there was evidence of micro cracks and defects in specimens.

- The EBSD local texture analysis of the tungsten specimens showed a <111> // Z preferential fibre texture, parallel to the build direction.